Deformation-induced martensitic transformation in Co-28Cr-6Mo alloy produced by laser powder bed fusion: comparison surface *vs.* bulk

L.H.M. Antunes[a], J.J. Hoyos[b], T.C. Andrade[c], P.W.C. Sarvezuk[d], L. Wu[e], J.A. Ávila[f], J.P. Oliveira[g 1], N. Schell[j], A.L. Jardini[h], J. Žilková[i], P.F. da Silva Farina[a], H.F.G. Abreu[c], M. Béreš[c,h]

[a] School of Mechanical Engineering, University of Campinas, Rua Mendeleyev, 200, 13083-860, Campinas, SP, Brazil

[b] Department of Mechanical Engineering, Faculty of Engineering, University of Buenos Aires. Av. Paseo Colón 850, (C1063ACV), CA Buenos Aires, Argentina

[c] Department of Metallurgical and Materials Engineering, Federal University of Ceará, Av. Humberto Monte, 60445-554, Fortaleza, CE, Brazil

[d] Department of Physics, Federal University of Technology - Paraná, Via Rosalina Maria dos Santos, 1233, 87301899 Campo Mourão, Brazil

[e] National Laboratory of Synchrotron Light – LNLS, CNPEM, R. Giuseppe Máximo Scolfaro 10000, 13083-970, Campinas, SP, Brazil

[f] UNESP São Paulo State University, São João da Boa Vista, SP, Brazil

[g] Department of Mechanical and Industrial Engineering, NOVA University of Lisbon, 2829-516 Caparica, Lisbon, Portugal

[h] National Institute of Biofabrication, Faculty of Chemical Engineering, University of Campinas, Av. Albert Einstein 500, 13083-852, Campinas, SP, Brazil

[I] Department of Electrical Engineering and Mechatronics, Technical University of Košice, Letná 9, 042 00 Košice, Slovak Republic

[j] Helmholtz-Zentrum Geesthacht, Institute of Materials Research, Max-Planck-Str. 1, Geesthacht 21502, Germany

Keywords: CoCrMo alloy, martensitic phase transformation, *in-situ* synchrotron X-Ray diffraction, peak broadening, variant selection

Statement on Conflicts of Interest: One of the authors of this article is part of the Editorial Board of the journal. To avoid potential conflicts of interest, the responsibility for the editorial and peer-review process of this article lies with the journal's other editors. Furthermore, the authors of this article were removed from the peer review process and had no, and will not have any access to confidential information related to the editorial process of this article.

Abstract

The wear resistance of the biomedical low-carbon Co-28Cr-6Mo (wt.-%) alloy is mostly determined by the onset and magnitude of the face-centered cubic to hexagonal close-packed deformation-induced martensitic phase transformation. In metal-on-metal joint bearings, local plastic deformation occurs on the surface and in the subsurface regions. This can cause deformation-assisted structural changes in the material, such as mechanical twinning and/or martensitic transformation. In the present work, we report the structural transition on the surface and bulk of a laser powder bed fusion additively manufactured Co-28Cr-6Mo alloy in response to externally imposed loading. This study was possible using synchrotron X-ray diffraction at two different energy levels. Our results revealed that from tensile deformation to fracture, the phase transformation kinetics and magnitude were marginally higher on the surface. During transformation, $\{200\}_{FCC}$ peak broadening was observed in the bulk and this was attributed to stacking fault accumulation.

1. Introduction

Additive manufacturing (AM) techniques, such as electron beam and/or laser powder bed fusion, are increasingly being employed to fabricate biomedical implants and dental components from Co-28Cr-6Mo precursor powders [1–3]. High wear resistance and high mechanical strength are two crucial criteria for alloys used for metal-on-metal joint replacements. When two bearing surfaces slide against each other, the load is carried by several asperities rather than across the entire surface [4,5]. Under high local contact stresses, these asperities can be plastically deformed and eventually torn off, producing particulate wear debris that can lead to wear abrasion [4]. The release of debris can cause adverse reactions, including metal hypersensitivity, inflammation, osteolysis, carcinogenicity, and neuropathy [6]. Owing to its high mechanical strength and wear resistance, the low-carbon Co-28Cr-6Mo (wt.-%) alloy, which complies with the ASTM F-75 standard, is the preferred alloy for articulating surfaces in joint replacements. The high strength and good wear resistance of this alloy system are attributed to the deformation-induced martensitic transformation from face-centered cubic (FCC) to hexagonal close-packed (HCP) [7–10]. Henceforth, the FCC and HCP phases are also referred to γ and ε, respectively.

The γ/ε interfaces formed during the phase transformation act as barriers for dislocation gliding and suppress strain localization. During displacive martensitic transformation, the applied stress state can bias the crystallographic variant of the product phase from the parent phase [11]. Below 850°C, the Co-28Cr-6Mo alloy has a negative stacking fault energy [12,13] and is therefore susceptible to deformation-induced martensitic transformation that can take place on the surface and in the subsurface layers in addition to the bulk.

Compared to materials fabricated by conventional processing routes, in the laser powder bed fusion (LPBF) process, superior mechanical properties and unique microstructural features are attained. This is mainly attributed to the fast solidification and high cooling rates (~10^5-10^6 K/s) [14] of the melt pool. Such non-equilibrium conditions lead to formation of small grains (10-100 μm) containing ultrafine solidification cells (< 1 μm) which are surrounded by dense dislocation walls contributing to mechanical strengthening [15,16]. In addition, Wang *et al. [14]* reported that in Co-Cr-Mo alloys fabricated via LPBF process, 95 vol.-% of athermal HCP phase was achieved. The high volume fraction of HCP phase was attributed to high density of dislocations and stacking faults formed by non-equilibrium rapid solidification. In contrast, cast material with an identical chemical

composition attained such volume fraction of HCP phase after heat treatment conducted. However, the authors did not report on the procedure used for the sample preparation. Therefore, the high volume fraction of HCP phase observed in their LPBF as-built specimen can be caused by deformation-induced martensitic transformation. Lu *et al. [15]* pointed out that the accumulation of the residual stress during the LPBF process resulted in the generation of overlapping stacking faults embryos by dissociating of perfect dislocation into a pair of Shockley partial dislocations promoting formation of the HCP phase. In stainless steel, Freeman *et al. [16]* observed the presence of a highly metastable retained austenite originated from the LPBF process. This was not reported previously in alloys produced by conventional fabrication methods.

The displacive γ → ε phase transformation in the Co-28Cr-6Mo alloy follows the Shoji-Nishiyama (S-N) orientation relationship: $\{111\}_\gamma$ // $\{0001\}_\varepsilon$ and $\langle 1\bar{1}0\rangle_\gamma$ // $\langle 2\bar{1}\bar{1}0\rangle_\varepsilon$ and during this transformation, the austenitic grain can transform into twelve ε-martensite variants [17]. These 12 variants originate from the initial parent γ-phase through a shear process. However, depending on the austenitic crystal orientation and its stress state, not all martensitic variants may occur. Bokros and Parker [18] found that favored martensite variants have habit planes that are nearly perpendicular to the active slip plane in γ. In addition, an external stress applied to the bulk specimen increases the lattice strain [19], which reduces the Gibbs free energy of the martensitic transformation, contributing to the variant selection [11,20,21].

The extent of the γ → ε phase transformation during plastic deformation has recently been analyzed using synchrotron light sources [1,19,22]. In addition, variant selection analyzes were previously carried out on low stacking fault energy alloys [23,24]. However, these studies did not compare characteristics of both the phase transition and the variant selection occurring on the surface and in the bulk. This is unprecedented in obtaining the comprehension of material behavior during service.

Here, we present the results of *in situ* tensile loading experiments using two synchrotron light sources with different energy levels, which allowed us to probe both the surface and bulk microstructural evolution of the as-built parts. We have identified the onset and kinetics of the deformation-induced phase transition in addition to the rate of lattice strain accumulation in both the bulk and the surface. Moreover, variant selection analysis revealed differences between the bulk and surface regions.

2. Material and methods

2.1 Material

MP1 alloy powder feedstock (EOS GmbH, Krailling, Germany), in compliance with the ASTM F-75 standard, was used to prepare tensile test specimens using an EOSINT M280 selective laser melting machine (EOS GmbH, Krailling, Germany). The machine was operated in a nitrogen atmosphere using standard process parameters for the MP1 alloy. Two specimens were fabricated for conventional tensile testing, and two samples were produced for *in situ* synchrotron X-ray measurements under load application. The cross-sectional areas of samples for conventional tensile testing and synchrotron X-ray diffraction load experiments were 6×2 mm^2 and 3.96×1.50 mm^2, respectively. Additional experimental details can be found in a previous study [19]. The chemical composition (wt.-%) of the produced samples was 27.89Cr-6.27Mo-0.72Mn-0.62Si-0.32Fe-0.1Ni-0.14C-0.14N, balance Co.

2.2 Tensile deformation

Tensile test specimens with a cross section of 6×2 mm^2 and 32 mm in gauge length, were deformed at room temperature in a strain control mode to 4% plastic strain on an MTS 810–FlexTest 40 servo-hydraulic testing machine. The strain rate used was 5×10^{-3} s^{-1}, and the average strain over a gauge length of 25 mm was recorded using an MTS 632.24C-50 extensometer. Mechanical properties including yield stress, ultimate tensile strength, and elongation at break, were obtained from tensile tests using experimental details reported in a previous paper [19].

Because the alloy of concern exhibits work hardening, the side surfaces of the fabricated tensile specimens were electropolished before tensile deformation. Electropolishing was performed using Struers Lectropol-5 equipment at 25 °C under 20 V tension using a solution of 10% perchloric acid in acetic acid. The surfaces of the deformed specimens were then subjected to microstructural characterization without the need for additional metallographic preparation. The bulk microstructure was obtained from the deformed tensile test specimen with 2 mm in thickness that was electropolished to a distance 1 mm from the surface.

2.3 Microstructural characterization

The electropolished as-built and deformed tensile test specimens were examined via field emission gun scanning electron microscopy (FEG-SEM) using FEI 650 and FEI 450 microscopes that were both fitted with electron backscattered diffraction (EBSD) detectors

(Nordlys, Oxford Instruments). The acceleration voltage used to acquire the EBSD maps was 15 kV and the step size was 0.1 μm.

For the nanoscale characterization, transmission electron microscopy (TEM) was used. Disc specimens that were 3 mm in diameter were cut from ~100 μm thick electrolytically thinned foils taken from both the as-built and 4% deformed tensile test specimens. The disc specimens were then further electropolished to obtain electron transparency using a Struers Tenupol-3 apparatus with the electrolyte and conditions mentioned previously. A JEOL FX2100 transmission electron microscope operated at 200 kV was utilized to acquire bright field micrographs.

2.4 Synchrotron X-ray diffraction experiments

Tensile test specimens with cross section of 3.96×1.5 mm^2 and 4.5 mm in gauge length were used in synchrotron X-ray diffraction systems that can impose mechanical load. The load was applied perpendicularly to the specimen's build direction at a strain rate of 10^{-3} s^{-1} while simultaneously acquiring X-ray diffraction patterns. Two synchrotron X-ray sources were utilized in this study, XRD1/XTMS beamline at the Brazilian Synchrotron Light Laboratory (LNLS) at the National Center for Research in Energy and Materials, Campinas/Brazil and P07/Petra III beamline at the German Electron Synchrotron (DESY), Hamburg/Germany. The beam size at the XRD1/XTMS and at the P07/Petra III beamline was 2×2 mm^2 and 1×1 mm^2, respectively. In both experimental trials, the beam size was larger than the average grain size measured in our specimens (i.e. ~ 40 μm).

1. The bulk crystal structure evolution was evaluated in transmission mode using high-energy X-ray diffraction at a wavelength of 0.1423 Å (87 kV). This ensures that several layers were captured and therefore, bulk information was obtained. Diffraction data were collected for 60 s using a 2D Mar345 detector, while the load was held constant at ~2.5% strain increments up to fracture. The strain value was determined from the crosshead displacement.
2. The crystal structures on the surface and in the subsurface regions were measured using X-ray diffraction at a wavelength of 1.034 Å (12 kV). Tensile loading experiments were performed by mounting the samples in a loaded rig of the GLEEBLE 3500 thermomechanical simulator, and the strain was measured using a laser extensometer. The load was held constant for 400 s at ~2% strain increments up to fracture, and diffraction patterns were simultaneously captured using two 1D Mythen detectors in the reflection mode.

To normalize the different energies from the synchrotron light sources, the full width at half maximum was calculated using the momentum transfer in reciprocal space (Q):

$$Q = \frac{4\pi \sin\theta}{\lambda} \quad (1)$$

where θ is the Bragg angle and λ is the wavelength, which is equal to 0.142 Å and 1.033 Å at beamlines P07/Petra III and XRD1/XTMS, respectively.

The lattice strain values (e) of the γ_{FCC} were estimated using the Stokes and Wilson methods.

$$e = \frac{\beta}{4\tan\theta} \quad (2)$$

β is the full width at half maximum expressed in radians, and θ is the Bragg angle [25].

The volume fractions of the γ and the ε phases were determined via Rietveld analysis using the FullProf software package. The space groups used in the refinement were $Fm\acute{3}m$ for the γ-phase and P63/mmc for the ε-phase, respectively. The only correction of the preferred orientation was performed on $\{111\}_\gamma$ planes, using the preferential plane parameter for this phase.

2.5. Variant selection analysis

The γ → ε transformation takes place in every second $(111)_\gamma$ plane that is displaced in the $[11\acute{2}]_\gamma$ direction by $\frac{a_\gamma}{\sqrt{6}}$ [18], causing the shear planes $(111)_\gamma$ to be parallel to the $(0001)_\gamma$ planes of the ε-martensite. Following these criteria, Patel-Cohen [17] developed a model to predict the interaction energy of $\gamma \rightarrow \alpha$ phase transformation and, consequently, predict variant selection. Later, Humbert [27] described $\gamma \rightarrow \alpha'$ a transition based on a two-step model with an intermediate phase (ε-martensite). Then, the α' -martensite variant selection can be estimated from the $\gamma \rightarrow \varepsilon \rightarrow \alpha'$ transformation. The two-step model has been omitted by several authors because the one-step model yielded the same results. However, Humbert's approach can be employed when the ε-martensite phase is of interest.

Kundu and Bhadeshia [21] showed that the Patel-Cohen [17] and Humbert [27] models differ by a factor of 0.5 because Humbert [27] assumed that the stress-strain relationship is

elastic; however, the transformation strain is plastic. According to Patel-Cohen [17], the interaction energy can be written as

$$W = \sigma\epsilon \quad (3)$$

where σ is the macroscopic stress-imposed tensor and ϵ is the transformation strain associated with the phase transformation. We used the Humbert model with a crystal reference frame to describe the phase transformation [28]. Therefore, for uniaxial stress, the interaction energy can be rewritten as:

$$W^{\gamma \rightarrow \varepsilon} = m\,\sigma_{11}\epsilon_{13} \quad (4)$$

where m is the Schmid factor for the $\{111\}_\gamma\langle 112\rangle_\gamma$ slip system, σ_{11} is the applied uniaxial stress, and ϵ_{13} is the pure shear transformation strain associated with the transformation, where $\epsilon_{13} = \epsilon_{31} = (2\sqrt{2})^{-1}$. Thus, the selected variants for ε-martensite are the variants with the highest Schmid factor. Finally, according to Humbert [27], only the variants with the maximum interaction energy were selected. Therefore, the variant with the highest energy was chosen, followed by the others that had energy in the range of 10% of the energy of this variant. This was the severity factor proposed by Humbert *et al.[27]*.

3. Results and discussion

A typical textured columnar microstructure formed in the as-built sample is shown in Figure 1. A single γ-phase was identified in this condition. The 4 % plastic deformation applied to the specimens caused the γ → ε phase transformation and formation of slip traces aligned within columnar grains, Figure 2a and c. In addition, these figures revealed that the extent of transformation on the surface was greater than that in the bulk. Please note, that the EBSD maps of the bulk specimen were collected from the deformed tensile test specimen (2 mm in thickness) that was electropolished 1 mm from the surface. Hegele *et al. [29]* pointed out that the extent of martensitic transformation on the surface may be enhanced in the presence of oxides. However, the XRD analysis performed in the current work did not reveal the existence of oxides. Therefore, other factors discussed in the following sections are considered to boost the kinetics of martensitic transformation on the surface.

LPBF specimens present considerable residual stresses owing to the non-equilibrium solidification conditions in which the material experienced after each layer is deposited [30]. When subjected to strain, part of this residual stress is relieved by the deformation-induced martensitic transformation, leaving a residual plastic strain caused by the volume expansion resulting from the γ → ε phase transformation [31]. This is manifested by the increased values of kernel average misorientation (KAM), as presented in Figures 2b and d. The KAM values of the ε-phase are higher and more evenly distributed in the bulk compared to the surface. The lower KAM values and their homogeneous distribution in the bulk (Figure 2d) indicate that the plastic strain occurring from the martensitic transformation is accommodated by more γ grains surrounding the newly nucleated ε-phase. The higher degree of misorientation and its heterogeneous distribution at the surface (Figure 2b) indicates that the plastic strain occurring from the martensitic transformation is accommodated by fewer γ grains surrounding the newly nucleated ε-phase. Here, a heterogeneous stress field is produced near grain boundaries owing to the grain boundary constraint and the impingement on the ε plates from the neighboring grains [32].

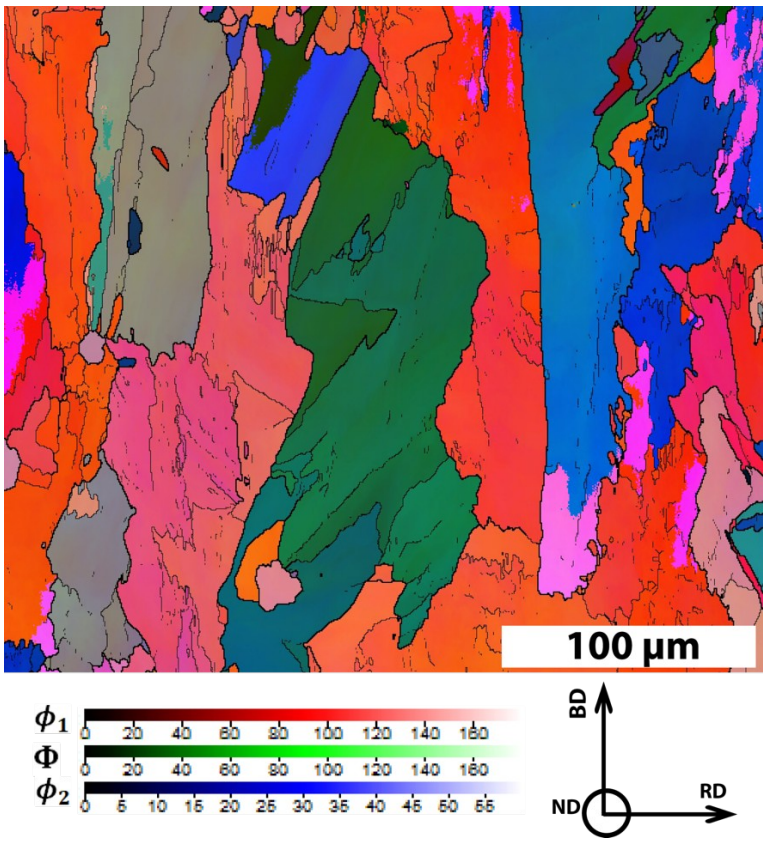

Figure 1 – EBSD Euler coloring map revealing columnar grains in the as-built sample.

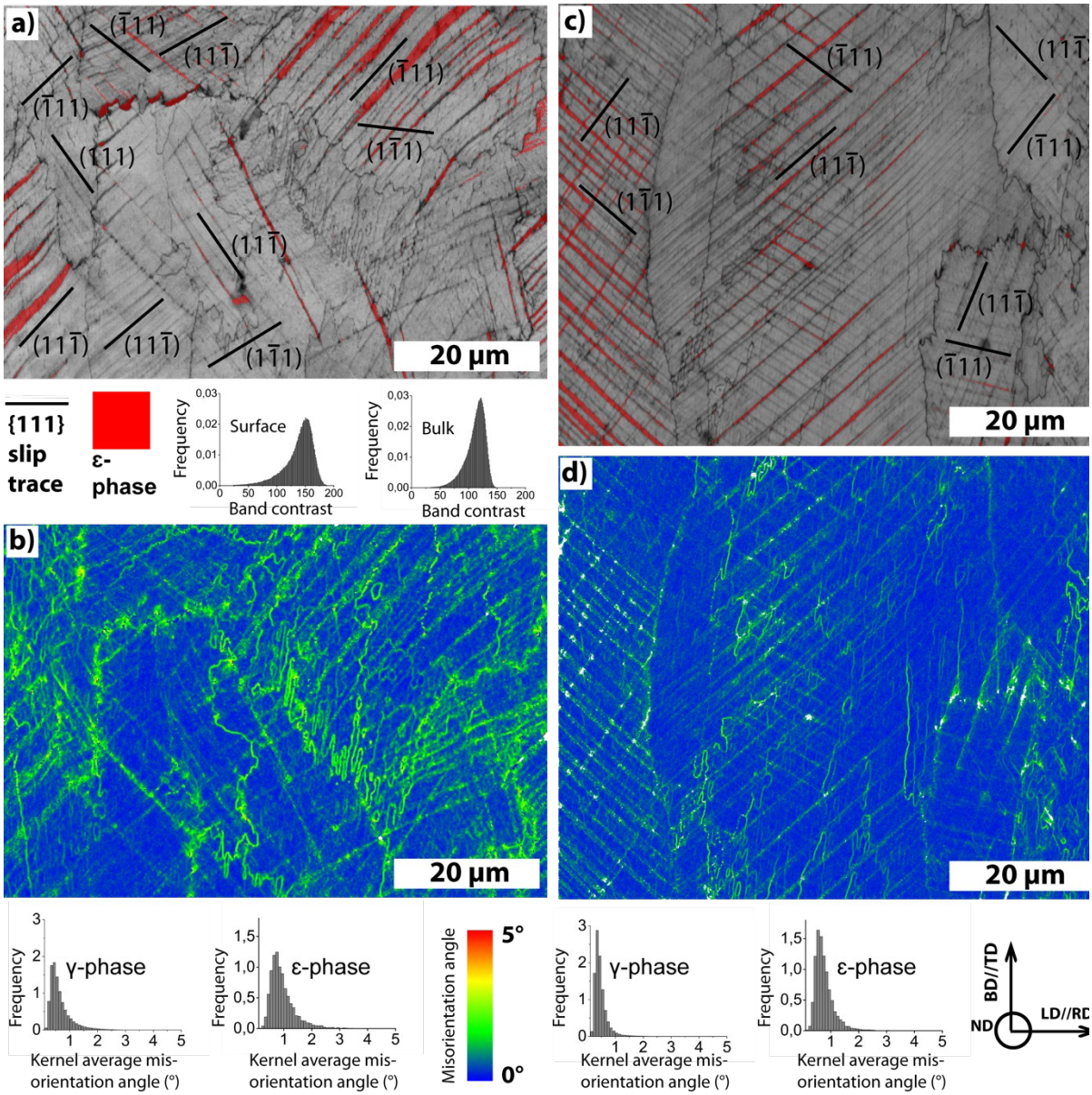

Figure 2 – EBSD phase and band contrast map collected after ~4% plastic deformation revealing the presence of deformation-induced ε martensite on the surface a) and in bulk, c), respectively. In these figures {111} slip traces are depicted. The corresponding kernel average misorientation maps are shown in b) and d). BD indicates build direction and LD indicates load direction.

Variant selection analysis was carried out using EBSD maps acquired from the bulk and the surface after tensile loading (refer to Figure 3). The orientation maps from the surface and bulk are shown in Figure 3a and d, respectively.

Figure 3b shows the experimentally determined pole figures for ε-martensite from the subset depicted in Figure 3a. Here, only one ε-martensite crystallographic variant was observed. Using a set of experimentally determined Euler angles from the γ-phase in the boxed region in Figure 3a, ε-martensite variants were calculated using the Humbert model presented in Section 2.5. The Euler angles used for the Humbert model were [297.8, 46.0, 28.9], and the resulting pole figures are shown in Figure 3c. One can note a good match

between the experimentally determined and simulated pole figures (Figure 3b and c). The same approach was applied to the bulk specimen, revealing good agreement between the experimentally determined and simulated pole figures (Figure 3e and f).

Table A.1 (Appendix A) shows the crystallographic variants for ε-martensite with orientation, Schmid factor, and interaction energy for each slip system. The selected variants were those with highest Schmid factors for Shockley partial dislocations. The experimental results of selected crystallographic variants and observed slip traces coincide with calculation results of the interaction energy for the martensitic transformation and Schmid factor values (detailed in Table A1).

Comparing the crystallographic variants present in bulk and surface, it was observed that the latter showed only one variant in the analyzed region, while in the bulk specimen, two variants were present. During the selection of certain crystallographic variants, variant shape deformation relieves the applied external stress.

In general, the deformation-induced martensitic transformation in FCC alloys is governed by the motion of Shockley partial dislocation pairs consisting of leading and trailing partials with different Schmid factors. The calculation of Schmid factors for perfect dislocation (m_p) in addition to leading partials (m_l¿ and trailing partials (m_t¿ showed the following: in most grains in which ε-martensite was detected, the Schmid factors of the leading partials (dislocations that form the ε-martensite) were lower than those of the trailing partials. Our analysis also revealed that the activated slip at the onset of plasticity was limited to the primary slip on one of the slip systems with the highest Schmid factors. Therefore, the γ → ε transformation is governed by the critical resolved shear stress (τ_{CRSS}) to activate the slip. Lee *et al*. [23] attributed this phenomenon to the negative-stacking fault energy in this alloy system. Consequently, isolated partial dislocations are preferred for the motion of the leading-trailing Shockley partial pairs. However, no ε-martensite variants were observed to be parallel to the load direction. This is because this orientation would decrease the resolved shear stress and then suppress the formation of ε-martensite variants [33].

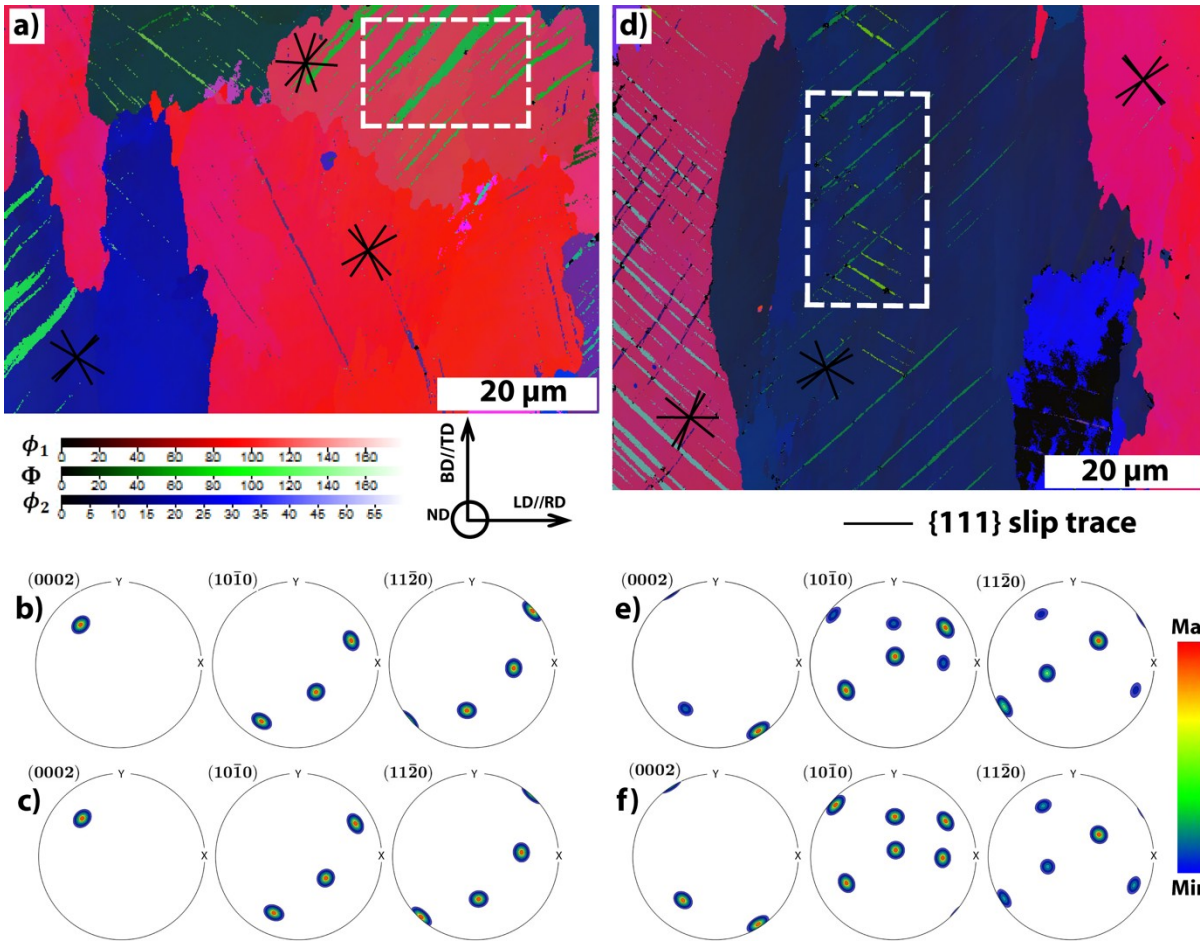

Figure 3 – Euler orientation maps collected from: a) surface and d) bulk. b) and e) are experimentally determined (0002), $(10\acute{1}0)$, and $(11\acute{2}0)$ pole figures of ε variants from boxed regions in a) and d) for surface and bulk specimens, respectively. c) and f) are calculated (0002), $(10\acute{1}0)$, and $(11\acute{2}0)$ pole figures of ε variants from boxed regions in a) and d) for surface and bulk specimens, respectively. BD indicates build direction and LD indicates load direction.

Zhang*et al*. [32] reported that the formation of variants with lower Schmid factors becomes more prominent as plastic deformation proceeds. Other factors, such as local stress concentration from martensite plates and inhomogeneous stresses near the boundary (as revealed in Figures 2b and d) may affect the deformation mode and variant selection [34].

A bright-field TEM image of the bulk specimen before deformation is shown in Figure 4a. Fringe contrasts from pre-existing stacking faults and their intersections can be observed. The majority of fringes terminated at the intersections of the $\{111\}_\gamma$ plane. The alloy of concern has a negative SFE [12] and is, therefore, susceptible to stacking fault formation. Figure 4b shows a bright-field TEM image of a sample subjected to ~4% plastic deformation. The presence of deformation-induced ε-martensite (depicted with an arrow) was observed in this condition. Under loading, the dislocation glide is inherently suppressed owing to the low stacking fault energy of the alloy. Consequently, slip is highly localized on pre-existing and strain-induced stacking faults with different crystallographic orientations. These regions form

various variants of deformation-induced ε-martensite in the loaded sample, as observed in Figure 3d. The measured misorientation angle between the two crystallographic variants of ε-martensite was ~71°. The γ→ε transformation follows the S-N orientation relationship: $\{111\}_\gamma$ // $\{0001\}_\varepsilon$ and $\langle 1\bar{1}0\rangle_\gamma$ // $\langle 2\bar{1}\bar{1}0\rangle_\varepsilon$. Therefore, different ε-martensite variants formed on one of the $\{111\}_\gamma$ planes can be obtained through the rotation of the basal plane by 71° in the corresponding $\langle 011\rangle_\gamma$ direction [35]. With increasing load, the ε-martensite plates deform plastically, leading to deviations in the misorientation angles.

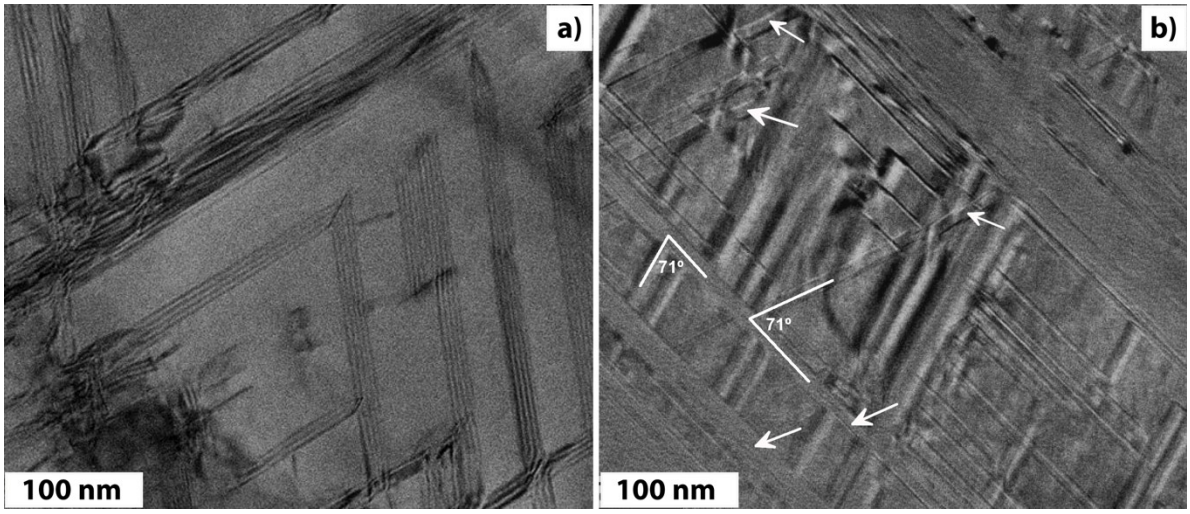

Figure 4 – Bright-field TEM micrographs showing stacking faults in non-deformed specimen a) and formation of deformation-induced ε-martensite (depicted with arrow) after ~ 4% plastic deformation in b).

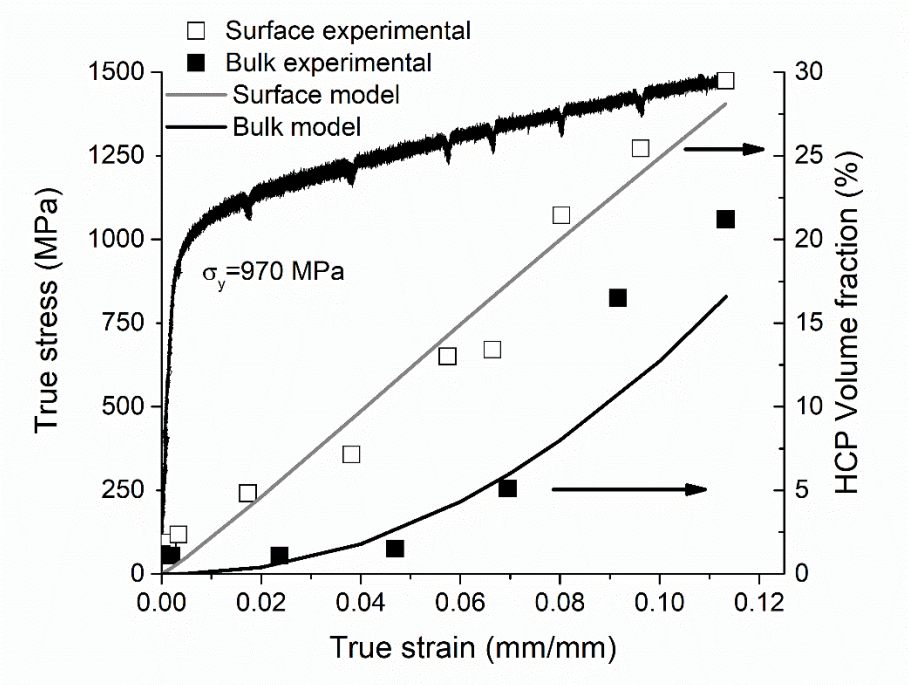

Figure 5 – True stress–true strain curve. Experimental and simulated kinetics of deformation-induced γ → ε phase transformation on surface and in bulk during tensile loading (beamline XTMS/LNLS Brazil and Petra III/DESY Germany).

The kinetics of the ε-phase during tensile deformation in bulk and on the surface were followed via the time-resolved XRD technique, using two synchrotron light sources, as shown in Figure 5. At the beginning of the loading, a single-phase γ-phase was identified. As the true strain increased, the γ → ε phase transformation started to occur. With increasing strain, the volumetric fraction of the ε-phase increased, and at a true strain of 0.115, it reached 21 and 30 vol.-% at the surface and in bulk, respectively.

The kinetics of the γ → ε phase martensitic transformation, presented in Figure 5, was estimated using Equation 5, which was proposed by Choi *et al*. [36]. Thus, the deformation-induced phase transformation acts as an effective relaxation process to relieve the internal strain energy accumulation during inelastic deformation.

$$V_\epsilon = V_s\left(1-\exp\left(-\beta\,\varepsilon^n\right)\right) \tag{5}$$

where V_ϵ is the volume fraction of ε-martensite, V_s is the saturation volume fraction of ε-martensite, β is a kinetic parameter that characterizes the stability of austenite, n represents the formation rate of nucleation sites, and ε is the strain (true or engineering).

Since the material of concern is composed of grains with average size of 40 μm, low energy X-ray results can be affected by surface effects, whereas high-energy results are not. In addition, calculation results of kinetics parameter, β, that characterizes the stability of austenite during martensitic transformation using model proposed by Choi *et al*. [36], Table1, revealed that the surface has a lower value of β than that of the bulk. This suggests that the surface has lower austenite stability when compared to the bulk.

With the use of synchrotron X-ray diffraction in transmission mode, bulk information averaged over the thickness of the sample was acquired allowing a volumetric evaluation of the bulk material free from surface effects. However, this information complements that obtained by surface characterization methods such as low energy X-ray diffraction or electron microscopy methods. Surface effects on martensitic transformation of several engineering alloys are well-know by now [37]. However, bulk residual stresses also play a role in this transformation. The issue is that LPBF process promotes the development of complex residual stresses that are not homogenous along the part. These non-homogenous residual stress patterns can then drastically modify the conditions of the martensitic transformation to occur. However, it is not possible to pin point yet what is the role of such residual stresses in the

martensitic transformation. For this to be evaluated, an in-situ measurement during the LPBF process needs to be performed. This, however, is beyond scope of the present paper and such measurement will be subject of further work.

Table 1 – Kinetics parameters of martensitic transformation in bulk and on surface using model proposed by Choi *et al*. [36].

Parameter	V_s	n	β
Surface	1	1.12	3.77
Bulk	1	2.20	21.55

Figure 6a shows the surface relief after 4% plastic deformation on the polished surface. In addition, surface cracking and melt-pool boundaries are visible. Figure 6b shows the side surface slip traces produced by the intersection of the $\{111\}$ slip planes with the polished side surface. These closely spaced slip steps produce facets with a lower pile-up height and coarsely spaced slip steps that produce higher pile-up heights. As shown on the left side of Figure 6b, the slip steps on the side surface indicate that unrelaxed pileups existed before the fracture. Therefore, the crack initiated at the piled-up dislocations on the surface toward the bulk. Figure 6b shows the fracture surface with the pile-up containing large slip steps, indicating a more ductile region in the bulk, as confirmed by the dimple structure along each slip step. The transformed γ-phase involves dense stacking faults, which effectively prevent dislocation movements in the γ-phase and contribute to the increase in the work-hardening rate [38]. Thus, at the interface between the γ and ε phases, there is strain incompatibility, leading to a stress concentration in this region. This stress concentration acts as a source of nucleation and microcrack growth as the plastic deformation continues. Therefore, it is likely that fractures originated at the surface of the specimen, which is in agreement with the work of Koizumi *et al*. [12]. Figure 6 also revealed formation of micro cracks at columnar grain boundaries. Therefore, in the LPBF material, there is strong texture sensitivity for plastic deformation, fracture initiation and formation of ε-martensite compared to that in equiaxed grains commonly observed in conventionally produced alloys (cast, forged and/or heat treated).

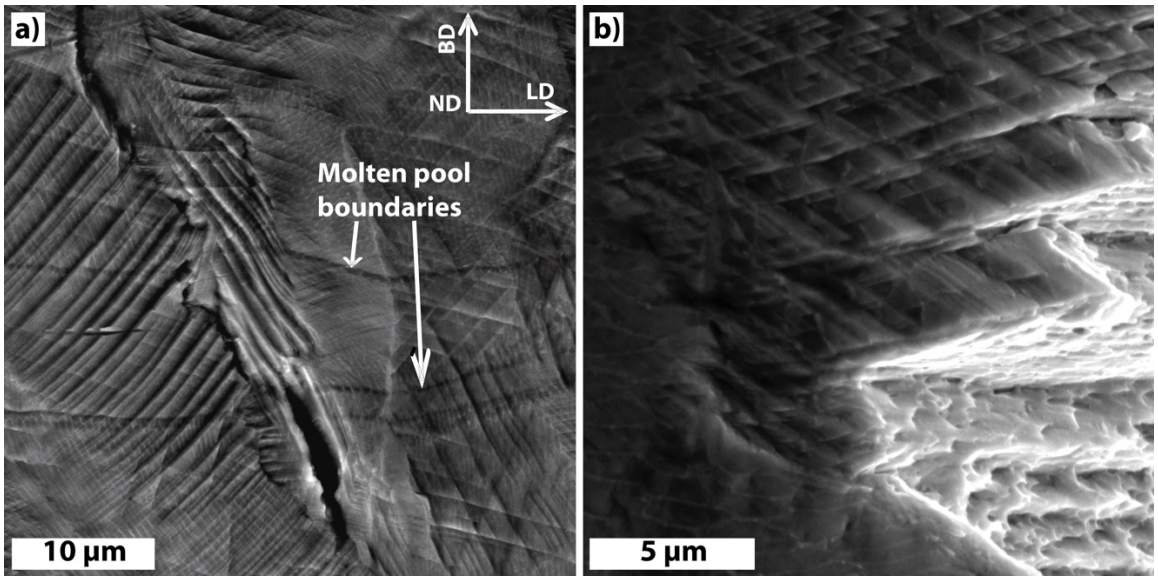

Figure 6 – a) Secondary electron micrograph acquired on pre-polished side surface of deformed tensile test specimen at distance of 30µm from fracture. b) On left side of image, pre-polished side surface of deformed tensile test specimen reveals pileups and slip traces produced by intersection of $\{111\}$ slip planes with previously polished side surface. On right side of image, slip steps at pileups on fracture facets are shown. BD indicates build direction and LD indicates load direction.

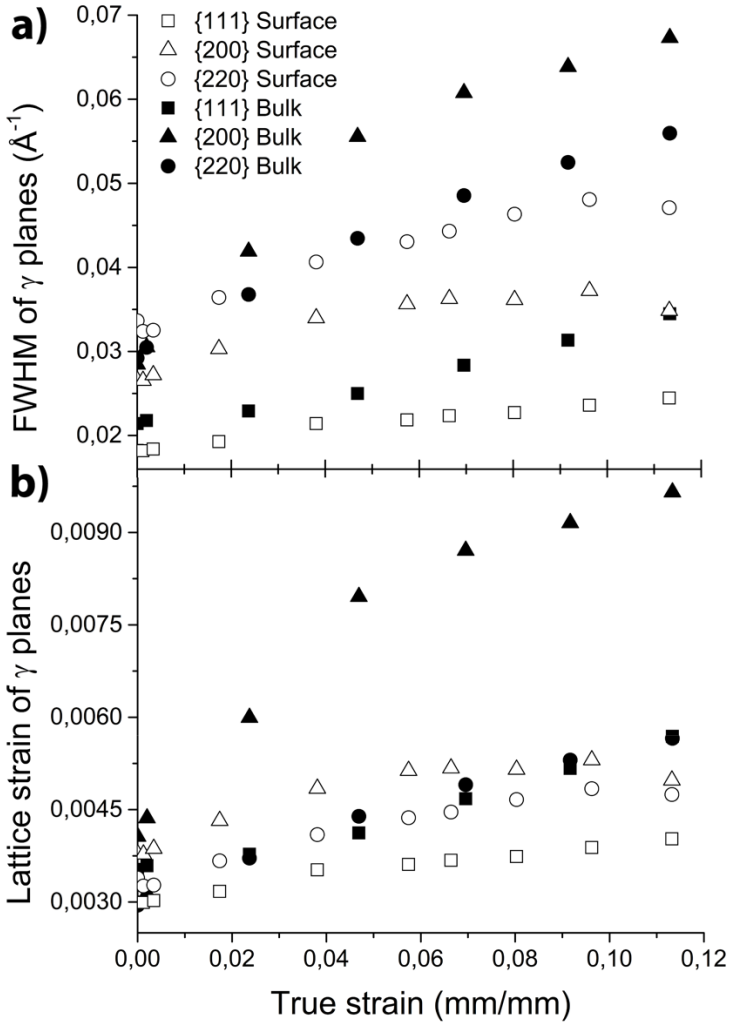

Figure 7 – a) Evolution of full width at half maximum as a function of true strain in tensile loaded specimen. Please note peak broadening in $\{200\}$ γ planes in bulk. b) Evolution of lattice strain in individual γ crystallographic planes as function of true strain in tensile loaded specimen.

On one hand, during tensile loading, significant peak broadening was observed in the $\{200\}_{\gamma}$ planes of the bulk specimen (refer to Figure 7a). The peak broadening is caused by the accumulation of stacking faults and back stresses in the neighboring grains with increasing strain. Here, large stress fields are produced near the grain boundaries owing to the grain boundary constraint and the impingement of the ε plates from the neighboring grains. On the other hand, no significant peak broadening was observed at the surface. Another reason for smaller $\{200\}_{\gamma}$ peak broadening at the surface could be explained in terms of the enhanced martensitic transformation at the surface, Figure 5. In general, the $\{200\}_{\gamma}$ peak is sensitive to dislocation density, causing more significant broadening. Mori *et al*. [39] argued that the ε-martensite is formed by consuming dislocations in the γ-matrix. In their work, synchrotron X-ray diffraction line-profile analysis was employed to track formation of ε-martensite and evolution of dislocation density during tensile deformation of multi-pass hot rolled Co-Cr-Mo alloy. During initial stages of tensile loading, the increase of the integral breadth of line profile was attributed to the rise of the dislocation density in the γ-matrix. At 0.2% proof stress, the dislocation density reached a maximum and ε-martensite started to form. With progressing plastic deformation, the observed reduction in dislocation density was attributed to the consumption of the dislocations in the γ-matrix during formation of ε-martensite. Results obtained by Mori *et al*. [39] are consistent with results presented in Figure 7, where one can observe an increase in the FWHM of the plane $\{200\}_{\gamma}$ in the initial stages of loading. With progressing loading, the rise in the FWHM can be associated with an increase in dislocation density. At the final stages of the plastic deformation, the FWHM starts to decrease, indicating the reduction of the dislocations density accompanied by formation of ε-martensite. One half of the Shockley partial pair marks the ε-phase, while the other half disappears at the surface, leaving behind a slip band. Indeed, because the surface of the specimen was polished prior to the plastic deformation, the formation of slip bands (and surface relief) on the deformed sample surface was observed (refer to Figures 2 and 6). Each band consists of a large number of slip steps equal to the Burgers vector $b=\frac{1}{6}\langle 1\acute{2}1\rangle$ on $\{111\}$ closely spaced parallel slip planes. Dislocations near the surface can escape and therefore do not accumulate the same back stresses in neighboring grains. Therefore, no

significant peak broadening was observed on the surface. For peak broadening, there is also an orientation dependence on the dislocation type [40,41].

In Figure 7b, it is possible to see the increase in lattice strain with increasing true strain for both the bulk and the surface. When comparing the surface to the bulk, the magnitude of the lattice strain was lower at the surface. The lattice strain is relieved by the formation of slip bands at the surface, as mentioned previously.

The higher lattice strain values contributed to the variant selection. Overall, the Gibb's energy (G) in the transformation comprises its chemical (ΔG_c) and mechanical (ΔG_m) contributions. The interaction energy U (Equation 6) is a significant contributor to ΔG_m and is a large fraction of the total $\Delta G = \Delta G_c + \Delta G_m$; variant selection can occur and contribute to G minimization occurring at equilibrium [11,42].

$$U = \sigma_N \zeta + \tau s \quad (6)$$

Where σ_N is the stress component normal to the habit plane; τ is the shear stress resolved on the habit plane in the direction of shear; and ζ and s are, respectively, the normal and shear strains associated with the transformation.

4. Conclusions

The characteristics of deformation-induced $\gamma_{FCC} \rightarrow \varepsilon_{HCP}$ phase transformation in a CoCrMo alloy fabricated by selective laser melting were investigated with two *in-situ* loading synchrotron-diffraction experiments. During monotonic tensile loading, different energy levels were employed to follow the phase transformation in the transmission mode (*i.e.*, in bulk) and reflection mode (*i.e.*, on the surface).

The following conclusions were drawn:

1- The accumulation rate of the ε-phase is higher on the surface than the bulk.
2- The formation of the ε-phase is associated with perfect dislocation slip for isolated Shockley partial dislocations rather than being governed by Schmid's law for Shockley leading-trailing partials.
3- Although the ε-phase is considered to improve the wear resistance in this alloy system, the γ/ε interfaces are sites for crack initiation and propagation.
4- The $\{200\}_\gamma$ peak broadening is associated with the accumulation of stacking faults with progressing strain.

Acknowledgments

The authors are grateful to Professor D. Dye from Imperial College London for his helpful discussions. The authors would like to acknowledge the experimental support of F.E. Montoro, Dr. C. Ospina, Dr. O.R. Bagnato, and Dr. A.L. Gobbi (projects SEM-26162, TEM-26161, LMF 20869) at the Brazilian Nanotechnology National Laboratory (LNNano). The assistance of J.L. Lisboa from Unicamp/Campinas with mechanical tests is also acknowledged. The research leading to this result has been supported by the project CALIPSOplus under the Grant Agreement 730872 from the EU Framework Programme for Research and Innovation HORIZON 2020 (proposal I-20160912)

This study used the resources of the Brazilian Synchrotron Light Laboratory (LNLS) (project 20170162), an open national facility operated by the Brazilian Center for Research in Energy and Materials for the Brazilian Ministry for Science, Technology, Innovations, and Communications.

Microstructural characterization of the specimens was performed at LNNano and the Analytical Center of UFC/CT-INFRA-FINEP/Pro-Equipamentos-CAPES/CNPq-SisNano-MCTI 2019(Grant 442577/ 2019-2)-INCT-FUNCAP. This study was financed in part by the Coordenação de Aperfeiçoamento de Pessoal de Nível Superior, Brasil, Finance Code 001, and Fundação para a Ciência e a Tecnologia (FCT - MCTES) via the project UIDB/00667/2020 (UNIDEMI).

References

[1] M. Béreš, C.C. Silva, P.W.C. Sarvezuk, L. Wu, L.H.M. Antunes, A.L. Jardini, A.L.M. Feitosa, J. Žilková, H.F.G. de Abreu, R.M. Filho, Mechanical and phase transformation behaviour of biomedical Co-Cr-Mo alloy fabricated by direct metal laser sintering, Mater. Sci. Eng. A. 714 (2018) 36–42. doi:10.1016/j.msea.2017.12.087.

[2] Y. Okazaki, Effects of fine microstructures and precipitates of laser-sintered Co–28Cr–6Mo alloy femoral components on wear rate of UHMWPE inserts in a knee joint simulator, J. Mech. Behav. Biomed. Mater. 112 (2020) 103998. doi:10.1016/j.jmbbm.2020.103998.

[3] B. Konieczny, A. Szczesio-Wlodarczyk, J. Sokolowski, K. Bociong, Challenges of Co–Cr Alloy Additive Manufacturing Methods in Dentistry—The Current State of

Knowledge (Systematic Review), Materials (Basel). 13 (2020) 3524. doi:10.3390/ma13163524.

[4] S.A. Brown, Chapter 2 - Synthetic Biomaterials for Spinal Applications, in: S.M. Kurtz, A.A.B.T.-S.T.H. Edidin (Eds.), Academic Press, Burlington, 2006: pp. 11–33. doi:https://doi.org/10.1016/B978-012369390-7/50003-4.

[5] M.A. Wimmer, J. Loos, R. Nassutt, M. Heitkemper, A. Fischer, The acting wear mechanisms on metal-on-metal hip joint bearings: In vitro results, Wear. 250–251 (2001) 129–139. doi:10.1016/S0043-1648(01)00654-8.

[6] N.J. Hallab, J.J. Jacobs, Biologic effects of implant debris, Bull. NYU Hosp. Jt. Dis. 67 (2009) 182–188.

[7] K. Yamanaka, M. Mori, Y. Koizumi, A. Chiba, Local strain evolution due to athermal γ→ε martensitic transformation in biomedical CoCrMo alloys, J. Mech. Behav. Biomed. Mater. 32 (2014) 52–61. doi:10.1016/j.jmbbm.2013.12.019.

[8] H. Kashani, A. Amadeh, A. Ohadizadeh, Effect of temperature on the strain induced γ → ε phase transformation in Stellite 21 during wear test, Mater. Sci. Eng. A. 435–436 (2006) 474–477. doi:10.1016/j.msea.2006.07.022.

[9] Y. Chen, Y. Li, S. Kurosu, K. Yamanaka, N. Tang, A. Chiba, Effects of microstructures on the sliding behavior of hot-pressed CoCrMo alloys, Wear. 319 (2014) 200–210. doi:10.1016/j.wear.2014.07.022.

[10] A. Chiba, K. Kumagai, N. Nomura, S. Miyakawa, Pin-on-disk wear behavior in a like-on-like configuration in a biological environment of high carbon cast and low carbon forged Co-29Cr-6Mo alloys, Acta Mater. 55 (2007) 1309–1318. doi:10.1016/j.actamat.2006.10.005.

[11] M. Béreš, H.F.G. Abreu, L.P.M. Santos, C.M. Davies, D. Dye, Effect of variant transformations in fusion zones of gas metal arc welds, Sci. Technol. Weld. Join. 20 (2015) 353–360. doi:10.1179/1362171815Y.0000000025.

[12] Y. Koizumi, S. Suzuki, K. Yamanaka, B. Lee, K. Sato, Y. Li, S. Kurosu, H. Matsumoto, A. Chiba, Strain-induced martensitic transformation near twin boundaries in a biomedical Co–Cr–Mo alloy with negative stacking fault energy, Acta Mater. 61 (2013) 1648–1661. doi:10.1016/j.actamat.2012.11.041.

[13] K. Yamanaka, M. Mori, S. Kurosu, H. Matsumoto, A. Chiba, Ultrafine grain refinement of biomedical Co-29Cr-6Mo alloy during conventional hot-compression deformation, Metall. Mater. Trans. A Phys. Metall. Mater. Sci. 40 (2009) 1980–1994. doi:10.1007/s11661-009-9879-0.

[14] Z. Wang, S.Y. Tang, S. Scudino, Y.P. Ivanov, R.T. Qu, D. Wang, C. Yang, W.W. Zhang, A.L. Greer, J. Eckert, K.G. Prashanth, Additive manufacturing of a martensitic Co–Cr–Mo alloy: Towards circumventing the strength–ductility trade-off, Addit. Manuf. 37 (2021) 101725. doi:10.1016/j.addma.2020.101725.

[15] Y. Lu, C. Yang, Y. Liu, K. Yang, J. Lin, Characterization of lattice defects and tensile deformation of biomedical Co29Cr9W3Cu alloy produced by selective laser melting, Addit. Manuf. 30 (2019) 100908. doi:10.1016/j.addma.2019.100908.

[16] F.S.H.B. Freeman, J. Sharp, J. Xi, I. Todd, Influence of solidification cell structure on the martensitic transformation in additively manufactured steels, Addit. Manuf. 30 (2019) 100917. doi:10.1016/j.addma.2019.100917.

[17] J.R. Patel, M. Cohen, Criterion for the action of applied stress in the martensitic transformation, Acta Metall. 1 (1953) 531–538. doi:10.1016/0001-6160(53)90083-2.

[18] J. Bokros, E. Parker, The mechanism of the martensite burst transformation in Fe□Ni single crystals, Acta Metall. 11 (1963) 1291–1301. doi:10.1016/0001-6160(63)90024-5.

[19] L.H.M. Antunes, J.J. Hoyos, E.B. Fonseca, M. Béreš, P.F. da Silva Farina, E.S.N. Lopes, A.L. Jardini, R.M. Filho, Effect of phase transformation on ductility of additively manufactured Co–28Cr–6Mo alloy: An in situ synchrotron X-ray diffraction study during mechanical testing, Mater. Sci. Eng. A. 764 (2019) 138262. doi:10.1016/j.msea.2019.138262.

[20] H.K.D.H. Bhadeshia, H. Abreu, S. Kundu, Calculation of crystallographic texture due to displacive transformations, Int. J. Mater. Res. 99 (2008) 342–346. doi:10.3139/146.101645.

[21] S. Kundu, H.K.D.H. Bhadeshia, Crystallographic texture and intervening transformations, Scr. Mater. 57 (2007) 869–872. doi:https://doi.org/10.1016/j.scriptamat.2007.06.056.

[22] R.T. Smith, T. Lolla, D. Gandy, L. Wu, G. Faria, A.J. Ramirez, S.S. Babu, P.M. Anderson, In situ X-ray diffraction analysis of strain-induced transformations in Fe- and Co-base hardfacing alloys, Scr. Mater. 98 (2015) 60–63. doi:10.1016/j.scriptamat.2014.11.003.

[23] B. Lee, Y. Koizumi, H. Matsumoto, A. Chiba, Collective behavior of strain-induced martensitic transformation (SIMT) in biomedical Co–Cr–Mo–N alloy polycrystal: An ex-situ electron backscattering diffraction study, Mater. Sci. Eng. A. 611 (2014) 263–273. doi:10.1016/j.msea.2014.05.071.

[24] I. Weißensteiner, M. Petersmann, P. Erdely, A. Stark, T. Antretter, H. Clemens, V. Maier-Kiener, Deformation-induced phase transformation in a Co-Cr-W-Mo alloy studied by high-energy X-ray diffraction during in-situ compression tests, Acta Mater. 164 (2019) 272–282. doi:https://doi.org/10.1016/j.actamat.2018.10.035.

[25] B.D.D. Cullity, Elements of x-ray diffraction, Second, Addison-Wesley Publishing Company Inc, New York, 1978. doi:978-0201089202.

[26] Z. Nishiyama, X-ray investigation of the mechanism of the transformation from face centered cubic lattice to body centered cubic, Sci. Rep. Tohoku Univ. 23 (1934) 637. https://ci.nii.ac.jp/naid/10012549836/en/.

[27] M. Humbert, B. Petit, B. Bolle, N. Gey, Analysis of the γ–ε–α′ variant selection induced by 10% plastic deformation in 304 stainless steel at −60°C, Mater. Sci. Eng. A. 454–455 (2007) 508–517. doi:https://doi.org/10.1016/j.msea.2006.11.112.

[28] D. Maréchal, Linkage between mechanical properties and phase transformations in a 301LN austenitic stainless steel, University of British Columbia, 2011. doi:https://dx.doi.org/10.14288/1.0071814.

[29] P. Hegele, J. Von Kobylinski, L. Hitzler, C. Krempaszky, E. Werner, In-situ XRD study of phase transformation kinetics in a co-cr-w-alloy manufactured by laser powder-bed fusion, Crystals. 11 (2021) 1–21. doi:10.3390/cryst11020176.

[30] B. Kemerling, J.C. Lippold, C.M. Fancher, J. Bunn, Residual stress evaluation of components produced via direct metal laser sintering, Weld. World. 62 (2018) 663–674. doi:10.1007/s40194-018-0572-z.

[31] C.C. Tasan, M. Diehl, D. Yan, C. Zambaldi, P. Shanthraj, F. Roters, D. Raabe, Integrated experimental-simulation analysis of stress and strain partitioning in multiphase alloys, Acta Mater. 81 (2014) 386–400. doi:10.1016/j.actamat.2014.07.071.

[32] X. Zhang, T. Sawaguchi, K. Ogawa, F. Yin, X. Zhao, Orientation dependence of variant selection and intersection reactions of ε martensite in a high-manganese austenitic steel, Philos. Mag. Lett. 91 (2011) 563–571. doi:10.1080/09500839.2011.596492.

[33] M.L. Benson, P.K. Liaw, H. Choo, D.W. Brown, M.R. Daymond, D.L. Klarstrom, Strain-induced phase transformation in a cobalt-based superalloy during different loading modes, Mater. Sci. Eng. A. 528 (2011) 6051–6058. doi:10.1016/j.msea.2011.03.096.

[34] N. Nakada, T. Tsuchiyama, S. Takaki, S. Hashizume, Variant Selection of Reversed Austenite in Lath Martensite, ISIJ Int. 47 (2007) 1527–1532. doi:10.2355/isijinternational.47.1527.

[35] J.H. Yang, C.M. Wayman, On secondary variants formed at intersections of ϵ martensite variants, Acta Metall. Mater. 40 (1992) 2011–2023. doi:10.1016/0956-7151(92)90187-J.

[36] H.C. Choi, T.K. Ha, H.C. Shin, Y.W. Chang, The formation kinetics of deformation twin and deformation induced ϵ-martensite in an austenitic Fe-C-Mn steel, Scr. Mater. 40 (1999) 1171–1177. doi:https://doi.org/10.1016/S1359-6462(99)00017-2.

[37] E. Cakmak, S.C. Vogel, H. Choo, Effect of martensitic phase transformation on the hardening behavior and texture evolution in a 304L stainless steel under compression at liquid nitrogen temperature, Mater. Sci. Eng. A. 589 (2014) 235–241. doi:10.1016/j.msea.2013.09.093.

[38] H. Won, K. Jung, S. Hwang, S. Kang, D. Kim, H.W. Lee, K. Jung, S. Hwang, S. Kang, D. Kim, Microstructure and mechanical anisotropy of CoCrW alloy processed by selective laser melting, Mater. Sci. Eng. A. 749 (2019) 65–73. doi:10.1016/j.msea.2019.02.013.

[39] M. Mori, K. Yamanaka, S. Sato, S. Tsubaki, K. Satoh, M. Kumagai, M. Imafuku, T. Shobu, A. Chiba, Tuning strain-induced γ-to-ε martensitic transformation of biomedical Co–Cr–Mo alloys by introducing parent phase lattice defects, J. Mech. Behav. Biomed. Mater. 90 (2019) 523–529. doi:10.1016/j.jmbbm.2018.10.038.

[40] T. Ungár, Strain broadening caused by dislocations, Mater. Sci. Forum. 278–281 (1998) 151–156. doi:10.4028/www.scientific.net/msf.278-281.151.

[41] L. Balogh, G. Ribárik, T. Ungár, Stacking faults and twin boundaries in fcc crystals determined by x-ray diffraction profile analysis, J. Appl. Phys. 100 (2006) 1–10. doi:10.1063/1.2216195.

[42] S. Kundu, K. Hase, H.K.D.H. Bhadeshia, Crystallographic texture of stress-affected bainite, Proc. R. Soc. A Math. Phys. Eng. Sci. 463 (2007) 2309–2328. doi:10.1098/rspa.2007.1881.

Appendix A

Table A.1 – Crystallographic variants for ε-martensite with orientation, interaction energy, and Schmid factor for Shockley partial dislocations from boxed region in Figures 2 a) and d) for surface and bulk specimen, respectively. The bolded numbers indicate the selected variants, which were those with highest Schmid factors for partial dislocations.

Variant	Slip System	Surface					Bulk				
		$[297.8\ 46.0\ 28.9]_\gamma$					$[40.8\ 31.4\ 34.6]_\gamma$				
		Euler Angles (°)			Interaction Energy (MJ/m^3)	Schmid Factor	Euler Angles (°)			Interaction Energy (MJ/m^3)	Schmid Factor
		ϕ_1	Φ	ϕ_2			ϕ_1	Φ	ϕ_2		
$V_{\varepsilon 1}$	$(111)[\bar{2}11]$	57.59	15.12	79.87	-30.33	-0.16	199.83	24.33	43.20	12.89	0.07
	$(111)[1\bar{2}1]$	57.59	15.12	199.87	-9.73	-0.05	199.83	24.33	163.20	-26.90	-0.14
	$(111)[11\bar{2}]$	57.59	15.12	319.87	40.05	0.21	199.83	24.33	283.20	14.02	0.07
$V_{\varepsilon 2}$	$(\bar{1}11)$ [211]	226.01	55.67	93.19	-51.26	-0.26	323.09	55.28	111.43	-2.52	-0.01
	$(\bar{1}11)[\bar{1}2\bar{1}]$	226.01	55.67	333.19	**92.76**	**0.48**	323.09	55.28	351.43	-71.00	-0.37
	$(\bar{1}11)[\bar{1}1\bar{2}]$	226.01	55.67	213.19	-41.50	-0.21	323.09	55.28	231.43	**73.52**	**0.38**
$V_{\varepsilon 3}$	$(1\bar{1}1)[\bar{2}\bar{1}1]$	351.67	76.22	195.37	26.34	0.14	102.82	65.42	184.30	43.40	0.22
	$(1\bar{1}1)$ [121]	351.67	76.22	75.37	-7.75	-0.04	102.82	65.42	64.30	-79.61	-0.41
	$(1\bar{1}1)[1\bar{1}\bar{2}]$	351.67	76.22	315.37	-18.59	-0.10	102.82	65.42	304.30	36.21	0.19
$V_{\varepsilon 4}$	$(11\bar{1})[\bar{2}1\bar{1}]$	104.53	80.60	341.67	-35.00	-0.18	212.30	94.27	335.41	**77.93**	**0.40**
	$(11\bar{1})[1\bar{2}\bar{1}]$	104.53	80.60	221.67	54.32	0.28	212.30	94.27	215.41	-73.77	-0.38
	$(11\bar{1})$ [112]	104.53	80.60	101.67	-19.32	-0.10	212.30	94.27	95.41	-4.16	-0.02